BNL-224201-2023-JAAM

# Mid-Infrared Nonlinear Frequency Conversion Using Monolithic Barium Titanate on Silicon-on-Insulator

J. Zhou, M. Liu

To be published in "IEEE Journal of Selected Topics in Quantum Electronics"

February 2023

Center for Functional Nanomaterials

**Brookhaven National Laboratory**

**U.S. Department of Energy**

USDOE Office of Science (SC), Basic Energy Sciences (BES) (SC-22)

# DISCLAIMER

# Mid-Infrared Nonlinear Frequency Conversion Using Monolithic Barium Titanate on Silicon-on-Insulator

Junchao Zhou, Mingzhao Liu, Chenyu Zhou, Bing Hau Kuo, Fuh-Sheng Shieu, Pao Tai Lin

***Abstract*— Efficient nonlinear frequency conversion in the mid-infrared (mid-IR) region was demonstrated by a barium titanate (BTO) on a silicon-on-insulator (SOI) substrate. The BTO thin film was epitaxially grown by pulsed-laser deposition (PLD). The tensorial second order optical nonlinearity and the ferroelectric domain property of the BTO were characterized by the polarimetric mid-IR second harmonic generation (SHG) measurements. Azimuthal-dependent polarized SHG was modeled at different combinations of the nonlinear coefficient $d_{ij}$ and the domain fraction factor $\Delta D^Y/\Delta D^X$. Strong SHG intensity was experimentally observed over a broad spectrum at λ = 3.1 µm - 3.7 µm. A characteristic linear dependence between the SHG signal and the square of the pumping laser intensity was observed. The monolithic integration between the epitaxial BTO and the Si provides a compact platform for efficient on-chip light generation and quantum photonic technologies.**

***Index Terms*—Mid-infrared, second harmonic generation, barium titanate, thin films**

## I. Introduction

COMPLEX metal oxides including $LiNbO_3$, $LaTiO_3$, and $BaTiO_3$ (BTO) with a perovskite crystal structure is critical in nonlinear photonics because of their large second order optical nonlinearity. The ferroelectricity and the optical nonlinearity of perovskite oxides are attributed to their non-centrosymmetric structure and transition-metal B cations [1]. The nonlinear response from the spontaneous dipole moment within a perovskite unit cell can result in photons that carry an energy different from the exciting laser. By mixing or splitting the energies from the incoming photons, coherent lightwave with specific wavelengths is created through various mechanisms, such as SHG, sum-and difference- frequency generation (SFG and DFG), and optical parametric oscillation (OPO). Bulk perovskite oxide single crystals have been utilized in various nonlinear photonic systems, including $LiNbO_3$ and $LaTiO_3$ based OPO and optical parametric amplification (OPA) [2,3]. Applying quasi-phase matching on these perovskite oxide crystals, nonlinear frequency conversion becomes more efficient and provides coherent light sources over a broad spectrum [4-6]. In addition, the nonlinear optical method can generate entangled photon-pair through parametric down-conversion, which is critical for the development of quantum communication and networking [7,8].

Nevertheless, compact devices desire perovskite oxides thin films over conventional bulk crystals for numerous chip-scale applications, such as electro-optic modulators [9], gas sensors [10], and non-volatile memory devices [11]. Deposition methods like atomic layer deposition (ALD), molecule-beam epitaxy (MBE), and chemical vapor deposition (CVD) have been explored to grow crystalline perovskite oxide thin films [12-15]. Among various candidates of nonlinear optical thin films, BTO has received significant attention for the applications in the integrated photonic circuits. BTO has the advantages of wide spectral transparency [16,17], strong Pockels effect [18,19], and high second-order optical nonlinearity [20]. To monolithically integrate BTO with present Si photonics, growth of epitaxial BTO thin films on Si substrates has been investigated through different deposition techniques [21,22]. For instance, thin TiN and MgO buffer layers were applied to reduce the large lattice mismatch between the BTO and the Si to enable monolithic BTO-on-Si platforms [23,24].

Though the visible and near-IR nonlinear coefficients $d_{ij}$ of BTO-on-Si have been measured [25-27], their mid-IR optical nonlinearity remains unknown. Mid-IR is critical because it overlaps with characteristic absorptions of numerous chemical functional groups, thus enabling label-free biomolecule sensing and non-destructive chemical detection [28-32]. In addition, the wide spectral range of mid-IR provides additional bandwidth for optical network and data transmission [33]. In this work, epitaxial BTO films was grown on a silicon-on-insulator (SOI) substrate with a strontium titanate (STO) buffer layer to reduce the lattice mismatch between BTO and Si. Azimuthal-dependent SHG was measured to resolve the tensorial 2nd optical nonlinearity and the ferroelectric domain structures. Our

This paragraph of the first footnote will contain the date on which you submitted your paper for review.

Junchao Zhou is with the Department of Electrical and Computer Engineering, Texas A&M University, College Station, TX 77843, United States (e-mail: Junchao.zhou@tamu.edu).

Mingzhao Liu is with the Center for Functional Nanomaterials, Brookhaven National Laboratory, Upton, New York 11973, United States (e-mail: mzliu@bnl.gov).

Chenyu Zhou is with the CFN/BNL and Department of Materials Science and Chemical Engineering, Stony Brook University, Stony Brook, NY 11794 USA (e-mail: chenyu.zhou@stonybrook.edu).

Bing Hau Kuo and Fuh-Sheng Shieu are with the Department of Materials Science and Engineering, National Chung Hsing University, Taichung 40227, Taiwan (e-mail: bhkuo2@dragon.nchu.edu.tw; fsshieu@dragon.nchu.edu.tw).

Pao Tai Lin is with the Department of Electrical and Computer Engineering and the Department of Material Science and Engineering, Texas A&M University, College Station, TX 77843 USA (e-mail: paolin@ece.tamu.edu)

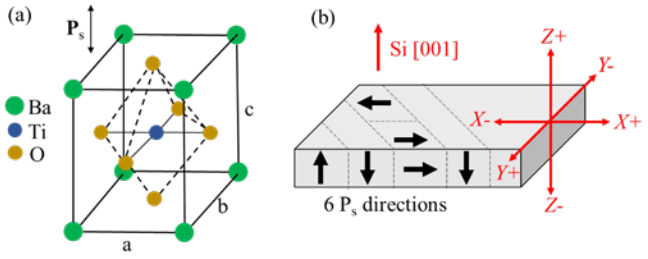


Fig. 1. (a) The BTO unit cell with Ti in the center, Ba in the corners, and O in the facet centers. The spontaneous polarization $\mathbf{P_s}$ is parallel to the c-axis. (b) The six ferroelectric domain orientations along the *X*+, *X*-, *Y*+, *Y*-, *Z*+, and *Z*- directions.

method provides the critical 2nd optical nonlinearity to the Si photonics and enables efficient frequency conversion. Hence, the BTO-on-Si platform provides a critical component for developing nonlinear mid-IR devices.

## II. Modeling of the Azimuthal Mid-IR SHG Patterns

BTO crystal has a non-centrosymmetric tetragonal phase at the temperature between 0 and 120 °C. Fig. 1 (a) illustrates the structure of a BTO crystal unit cell, where the O atoms are placed in the face-centered position and surround a Ti atom. A spontaneous polarization $\mathbf{P_s} \parallel$ c-axis is introduced when the Ti atom is deviated from the center of the unit cell along the c-axis [34,35]. Fig. 1 (b) is an illustration of the possible domain structure of a BTO thin film deposited on the Si (001) layer. The tetragonal BTO belongs to the 4mm point group. It has six domain variants, including $X+$, $X-$, $Y+$, $Y-$, $Z+$, and $Z-$, where the corresponding polarization $\mathbf{P_s}$ points into different directions. The tensor product between the 2nd order nonlinear coefficient $d_{ij}$ and the column associated with electric field component $\mathbf{E}$ determines the 2nd order nonlinear polarization $\boldsymbol{P}$ in (1):

$$\boldsymbol{P} = \begin{pmatrix} P_1 \\ P_2 \\ P_3 \end{pmatrix} = \begin{pmatrix} 0 & 0 & 0 & 0 & d_{15} & 0 \\ 0 & 0 & 0 & d_{15} & 0 & 0 \\ d_{31} & d_{31} & d_{33} & 0 & 0 & 0 \end{pmatrix} \begin{pmatrix} E_1^2 \\ E_2^2 \\ E_3^2 \\ 2E_2E_3 \\ 2E_1E_3 \\ 2E_1E_2 \end{pmatrix} \quad (1)$$

$E_1$, $E_2$, and $E_3$ are the electrical field components along $V_1$, $V_2$, and $V_3$ directions that define the coordination system of the ferroelectric domains. In addition, the $V_3$ axis is always along the dipole polarization direction. According to Zhou and Lin *et. al.* [36], the SHG intensity $I^{2\omega}$ of a multi-domain BTO thin film can be modelled by its tensorial component $d_{ij}$ and the domain fraction factor $\Delta D^Y/\Delta D^X$, where $\Delta D$ is the difference of the area ratio between a domain pair. For instance, $\Delta D^Y = D^{Y+} - D^{Y-}$, whereas $D^{Y+}$ and $D^{Y-}$ are the domain area ratios oriented along the $Y+$ and $Y-$ directions, respectively. The SHG intensity at the frequency of $2\omega$ along the *X*-polarization, $I_X^{2\omega}$, is proportional to $P_X^{2\omega}(P_X^{2\omega})^*$ and can be found by (2):

$$I_X^{2\omega} \propto (\Delta D^X)^2(d_{31}\sin^2\theta + d_{33}\cos^2\theta)^2 + (\Delta D^Y)^2(d_{15}\sin 2\theta)^2 + 2\Delta D^X \Delta D^Y(d_{31}\sin^2\theta + d_{33}\cos^2\theta)d_{15}\sin 2\theta\cos(\Gamma) \quad (2)$$

$\theta$ is the azimuthal angle between the linearly polarized incident light and the *X*-axis, $\Gamma = (2\pi L/\lambda)(n_c^{2\omega} - n_a^{2\omega})$, $L$ is the BTO thickness, and $n_c^{2\omega}$ and $n_a^{2\omega}$ are the refractive indexes along the c- and a- axes. The *Y*-polarized SHG intensity, $I_Y^{2\omega}$, can also be calculated through the same method. From Eq. (2), the SHG intensity is determined by the domain fraction difference $\Delta D$ and the coefficient $d_{ij}$, thus creating azimuthally symmetric SHG profiles. To illustrate the effect from the domain structure and the optical nonlinearity on mid-IR SHG, azimuthal $I_X^{2\omega}(\theta)$

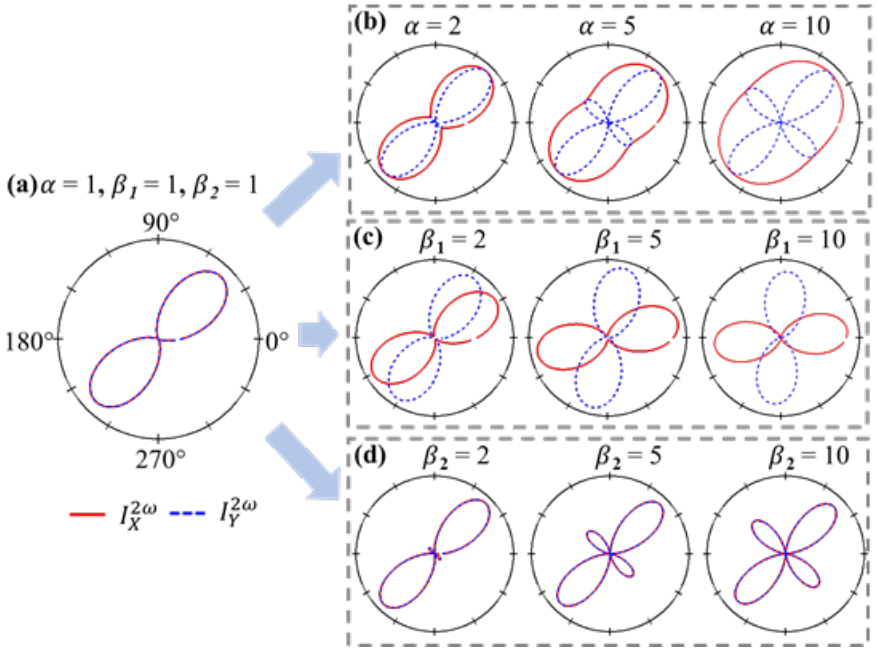


Fig. 2. The calculated azimuthal $I_X^{2\omega}(\theta)$ and $I_Y^{2\omega}(\theta)$. $\alpha$ is the domain fraction factor; $\beta_1$ and $\beta_2$ are the ratios between the nonlinear coefficients. (a) $\alpha = 1$, $\beta_1 = 1$, and $\beta_2 = 1$. (b) $\alpha$ increases from 2 to 10. $\beta_1 = 1$ and $\beta_2 = 1$. (c) $\beta_1$ increases from 2 to 10. $\alpha = 1$ and $\beta_2 = 1$. (d) $\beta_2$ increases from 2 to 10. $\alpha = 1$ and $\beta_1 = 1$.

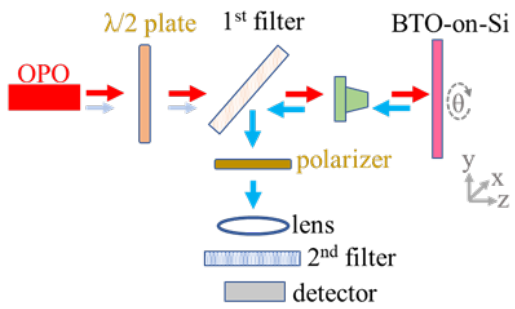


Fig. 3. The experimental setup to measure the azimuthal $I_X^{2\omega}(\theta)$ and $I_Y^{2\omega}(\theta)$ from the BTO-on-Si sample.

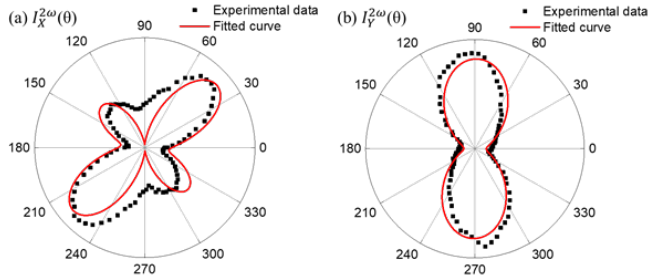


Fig. 4. The measured (a) $I_X^{2\omega}(\theta)$ and (b) $I_Y^{2\omega}(\theta)$ from the BTO-on-Si sample. $d_{15}$ = 9.5 pm/V, $d_{31}$ = 5.4 pm/V, $d_{33}$ = 15 pm/V, and $\Delta D^Y/\Delta D^X$= 24 were obtained from the fitting.

and $I_Y^{2\omega}(\theta)$ at the different domain fraction and the ratio between the tensorial nonlinearity were calculated and plotted in Fig. 2. Here, the parameter associated with the domain orientation is defined as $\alpha = \Delta D^X/\Delta D^Y$, and the ratios between the tensorial nonlinear coefficients are $\beta_1 = d_{33}/d_{31}$ and $\beta_2 = d_{15}/d_{31}$. In the initial condition $\alpha = 1$, $\beta_1 = 1$, and $\beta_2 = 1$, $I_X^{2\omega}(\theta)$ and $I_Y^{2\omega}(\theta)$ drawn in Fig. 2 (a) are overlapped and both show a symmetric two-lobed pattern because of the identical domain fraction along the *X* and *Y* orientations. In Fig. 2 (b), as $\alpha$ increases and the domain distribution between those two orientations is unequal, the center of $I_X^{2\omega}(\theta)$ plot becomes broader and additional two lobes are found in $I_Y^{2\omega}(\theta)$. At $\alpha$ = 10 , the $I_X^{2\omega}(\theta)$ shows an elliptic profile instead of a two-lobed pattern. Meanwhile, the deviation of $\beta_1$ from one rotates the two-lobed $I_x^{2\omega}(\theta)$ and $I_y^{2\omega}(\theta)$ in opposite directions. As displayed in Fig. 2 (c), $I_X^{2\omega}(\theta)$ rotates clockwise while $I_Y^{2\omega}(\theta)$ rotates counterclockwise as $\beta_1$ increases. The pattern of $I_X^{2\omega}(\theta)$ turns into perpendicular to $I_Y^{2\omega}(\theta)$ when $\beta_1$ reaches 10. Hence, the ratio between the tensorial coefficient $d_{ij}$ is critical in forming the angle dependent SHG profile. On the other hand, the increase of $\beta_2$ illustrated in Fig. 2 (d) converts the two-lobed $I_X^{2\omega}(\theta)$ and $I_Y^{2\omega}(\theta)$ to a four-lobed profile without rotating the SHG patterns. In addition, $I_X^{2\omega}(\theta)$ and $I_Y^{2\omega}(\theta)$ remains overlapped as $\beta_2$ changes. Therefore, the domain fraction factors and the tensorial nonlinear coefficients can be extrapolated by analyzing the azimuthal dependent SHG patterns.

## III. Experimental Results and Discussion

### A. BTO-on-Si Thin Film Deposition

A 100 nm thick STO buffer layer was first deposited on a SOI substrate by PLD and then followed by the BTO deposition. The SOI substrate has a 70 nm thick Si device layer and a 2000 nm thick $SiO_2$ layer. The deposition was carried out under 20 mTorr $O_2$ and the substrate was heated at 700°C. The PLD was equipped with a λ = 248 nm KrF excimer laser with a 1.5 J/cm$^2$ fluence and a 5 Hz repetition rate.

### B. Experimental Setup for Mid-IR SHG Characterization

The setup to characterize the SHG profile of a BTO-on-Si sample is illustrated in Fig. 3. The excitation light was from an optical parametric oscillators (OPO) laser with a 1 kHz pulse repetition rate and a 10 cm$^{-1}$ laser linewidth. A half-wave plate was placed right after the laser to control the polarization of the laser light. A filter transmitting light between λ = 3.25 and 3.75 μm was used to remove unwanted near-IR light from the OPO laser and also used as a beam splitter. After the filter, an objective lens was used to focus the incident light onto the BTO surface and also to collect the SHG signal from the sample. The laser light propagated in the *Z*-direction. The BTO-on-Si device was held onto a rotatable plate with an initial geometry of $X$ // $[100]_{Si}$, $Y$ // $[010]_{Si}$, and $Z$ // $[001]_{Si}$, then rotated by an angle θ. A broadband polarizer was placed next to the filter that separated the two orthogonally polarized SHG, $I_X^{2\omega}$ and $I_Y^{2\omega}$. The extinction ratio of the wire-grid polarizer was 10:1. Another filter transmitting light at λ = 1.5 - 2.0 μm was placed between the lens and the detector to block the residual excitation laser light. The SHG signal collected at different azimuthal angle θ was monitored by the detector connected with an oscilloscope for analysis.

### C. Measurement of Mid-IR Optical Nonlinearity and Domain Fraction Factor

Fig. 4 displays the azimuthal dependent SHG by rotating the BTO-on-Si sample with an angle θ, where $I_X^{2\omega}(\theta)$ and $I_Y^{2\omega}(\theta)$ present the SHG signals collected upon *X*-polarized and *Y*-polarized mid-IR excitation, respectively. For $I_X^{2\omega}(\theta)$ drawn in Fig. 4 (a), a four-lobed pattern with two main lobes point at θ = 45° and 225° are found. On the other hand, $I_Y^{2\omega}(\theta)$ drawn in Fig. 4 (b) shows a two-lobed profile. Comparing to the calculated SHG patterns in Fig. 2, the observed four-lobed $I_x^{2\omega}(\theta)$ and two-lobed $I_y^{2\omega}(\theta)$ indicate the BTO thin film has a large domain fraction factor. By fitting the polarimetric θ-dependent SHG, $d_{15}$ = 9.5 pm/V, $d_{31}$ = 5.4 pm/V, $d_{33}$ = 15 pm/V, and $\Delta D^Y/\Delta D^X$= 24 was resolved. For bulk BTO crystal, it has optical nonlinear coefficients of $d_{15}$ = 17 pm/V, $d_{31}$ =

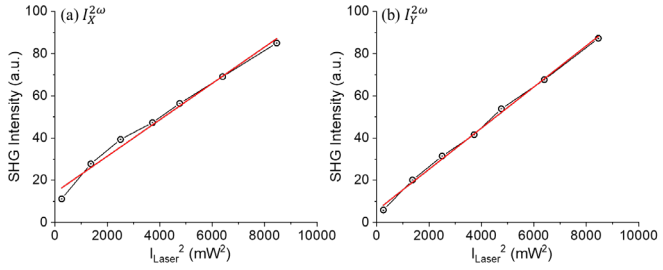


Fig. 5. The plots of (a) $I_X^{2\omega}(\theta)$ and (b) $I_Y^{2\omega}(\theta)$ versus $(I^\omega)^2$ at λ = 3.5 μm. A linear dependence between $I_{X,Y}^{2\omega}$ and $(I^\omega)^2$ was found.

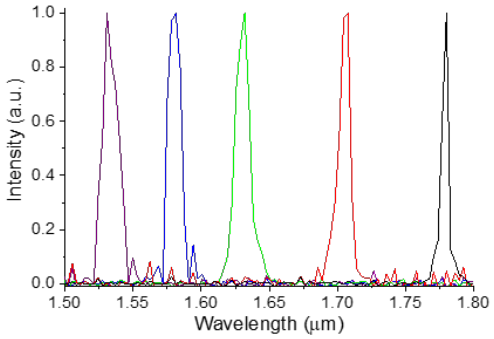


Fig. 6. The SHG spectrum of the BTO-on-Si sample when the pumping wavelength was shifted between $\lambda^{\omega}$ = 3.0 and 3.6 μm. Strong SHG was obtained over a broad spectrum.

15.7 pm/V, and $d_{33}$ = 6.8 pm/V. The difference of the nonlinear coefficients between a bulk crystal and the epitaxial film is caused by the strain between the BTO and the Si layer. Other complex oxides like $BaZrO_3$ showed the same epitaxial strain during the thin film deposition [37].

### *D. Mid-IR SHG vs. Excitation Laser Power and Wavelength*

The SHG intensity at different excitation laser power was recorded and drawn in Fig. 5. The laser wavelength was fixed at λ = 3.5 μm and the power was gradually increased from 16 to 92 mW. $I_X^{2\omega}$ was measured at $\theta = 45°$ in Fig. 5 (a) because it reached its maximum according to Fig. 4 (a). Similarly, $I_Y^{2\omega}$ in Fig. 5 (b) was measured at its maximum at $\theta = 90°$. Both $I_X^{2\omega}$ and $I_Y^{2\omega}$ plots show that the SHG intensity is linearly proportional to the square of the Mid-IR excitation light $(I^{\omega})^2$, which is the characteristic response from the 2nd order nonlinear optical process. Meanwhile, to measure the SHG spectrum, the detector in Fig. 3 was replaced by a spectrometer consisting of an InGaAs array. The excitation laser wavelength was adjusted from $\lambda^{\omega}$ = 3.0 to 3.6 μm, while the angle θ and the position of the BTO-on-Si remained the same. From Fig. 6, the SHG center wavelength consistently shifted from $\lambda^{2\omega}$ = 1.5 to 1.8 μm according to the excitation mid-IR wavelength. A wider SHG spectrum is found at $\lambda^{2\omega}$ < 1.6 μm because of the broadening of the excitation laser linewidth. The wide tuning range of the mid-IR SHG indicates the BTO-on-Si is a suitable platform to provide chip-scale light source.

## IV. Conclusions

Broadband mid-IR nonlinear light conversion was achieved by an epitaxial BTO-on-Si thin film from PLD. The azimuthal-dependent SHG patterns $I_x^{2\omega}(\theta)$ and $I_y^{2\omega}(\theta)$ were modelled at different ferroelectric domain fraction, $\alpha$, and various ratio between the nonlinear coefficients, $\beta_{1,2}$. As $\alpha$ increases, the two-lobed $I_x^{2\omega}(\theta)$ pattern reshaped to an elliptic profile, while the two-lobed $I_y^{2\omega}(\theta)$ converted to a four-lobed profile. On the other hand, the increase of $\beta_1$ rotated the $I_x^{2\omega}(\theta)$ and $I_y^{2\omega}(\theta)$ patterns in the opposite direction. By fitting the experimental observed SHG patterns, we demonstrated that the grown BTO thin film possessed large 2nd order optical nonlinearity with $d_{15}$ = 12.5 pm/V, $d_{31}$ = 9.0 pm/V, and $d_{33}$ = 10.0 pm/V, over a broad spectral range at λ = 3.0 - 3.6 μm. The monolithically integrated BTO-on-Si enables a platform for mid-IR nonlinear photonic circuits and optical quantum computing.

## Acknowledgment

The authors appreciate the support from Texas A&M University Presidential X-Grant and NSF-ERC PATHS-UP Program. The devices were characterized at the Mid-Infrared Integrated Photonics and Remote Sensing (MiPRoS) Laboratory. This research used resources of the Center for Functional Nanomaterials (CFN), which is a U.S. DOE Office of Science User Facility, at Brookhaven National Laboratory under Contract No. DE-SC0012704.

## References

[1] R. E. Cohen, "Origin of ferroelectricity in perovskite oxides," *Nature*, vol. 358, no. 6382, pp. 136-138, 1992.
[2] L. Arizmendi, "Photonic applications of lithium niobate crystals," *Physica Status Solidi (a)*, vol. 201, no. 2, pp. 253-283, 2004.
[3] X. Liang *et al*., "Compact chirped pulse optical parametric amplifier in periodically poled $LiTaO_3$," in *2005 Quantum Electronics and Laser Science Conference*, 2005, vol. 3: IEEE, pp. 1636-1638.
[4] A. Hermans *et al.,* "On the determination of χ(2) in thin films: a comparison of one-beam second-harmonic generation measurement methodologies," *Sci. Rep.*, vol. 7, no. 1, pp. 1-13, 2017.
[5] L. E. Myers *et al.*, "Quasi-phase-matched optical parametric oscillators in bulk periodically poled $LiNbO_3$," *JOSA B*, vol. 12, no. 11, pp. 2102-2116, 1995.
[6] M. A. Belkin *et al.*, "Terahertz quantum-cascade-laser source based on intracavity difference-frequency generation," *Nature Photonics,* vol. 1, no. 5, pp. 288-292, 2007.
[7] X. Lu *et al.*, "Chip-integrated visible–telecom entangled photon pair source for quantum communication," *Nature physics,* vol. 15, no. 4, pp. 373-381, 2019.
[8] I. Marinković *et al.*, "Hybrid integration of silicon photonic devices on lithium niobate for optomechanical wavelength conversion," *Nano Lett.,* vol. 21, no. 1, pp. 529-535, 2021.
[9] A. J. Mercante *et al.*, "110 GHz CMOS compatible thin film $LiNbO_3$ modulator on silicon," *Opt. Express,* vol. 24, no. 14, pp. 15590-15595, 2016.
[10] N. Setter *et al.*, "Ferroelectric thin films: Review of materials, properties, and applications," *J. Appl. Phys.,* vol. 100, no. 5, pp. 051606, 2006.
[11] W. Lee *et al.*, "Flexible graphene–PZT ferroelectric nonvolatile memory," *Nanotechnology,* vol. 24, no. 47, pp. 475202, 2013.
[12] J. Wang *et al.*, "Epitaxial $BiFeO_3$ multiferroic thin film heterostructures," *Science,* vol. 299, no. 5613, pp. 1719-1722, 2003.
[13] K. Suzuki *et al.*, "Ferroelectric property of alkoxy-derived $YMnO_3$ films crystallized in argon," *JPN J. Appl. Phys.,* vol. 42, no. 9R, pp. 5692, 2003.
[14] S. Raghavan *et al.*, "High-mobility $BaSnO_3$ grown by oxide molecular beam epitaxy," *APL Mater.,* vol. 4, no. 1, pp. 016106, 2016.
[15] E. Østreng *et al.*, "Atomic layer deposition of ferroelectric $LiNbO_3$," *J. Mater. Chem. C,* vol. 1, no. 27, pp. 4283-4290, 2013.
[16] Y. Garbovskiy, and A. Glushchenko, "Optical/ferroelectric characterization of $BaTiO_3$ and $PbTiO_3$ colloidal nanoparticles and their applications in hybrid materials technologies," *Appl. Opt.,* vol. 52, no. 22, pp. E34-E39, 2013.
[17] M. K. Trivedi *et al.*, "Impact of biofield treatment on atomic and structural characteristics of barium titanate powder," *Ind. Eng. Manag.,* vol. 4, no. 3, pp. 1000166, 2015.
[18] P. Lin, Z. Liu, and B. W. Wessels, "Ferroelectric thin film photonic crystal waveguide and its electro-optic properties," *J. Opt. A: Pure Appl. Opt.,* vol. 11, no. 7, pp. 075005, 2009.
[19] A. Petraru *et al.*, "Ferroelectric $BaTiO_3$ thin-film optical waveguide modulators," *Appl. Phys. Lett.,* vol. 81, no. 8, pp. 1375-1377, 2002.
[20] T. Zhao *et al.*, "Stress-induced enhancement of second-order nonlinear optical susceptibilities of barium titanate films," *J. Appl. Phys.,* vol. 87, no. 10, pp. 7448-7451, 2000.

[21] M. B. Lee *et al.*, "Heteroepitaxial growth of $BaTiO_3$ films on Si by pulsed laser deposition," *Appl. Phys. Lett.,* vol. 66, no. 11, pp. 1331-1333, 1995.
[22] M.-H. M. Hsu *et al.*, "Controlled orientation of molecular-beam-epitaxial BaTiO3 on Si (001) using thickness engineering of $BaTiO_3$ and $SrTiO_3$ buffer layers," *Appl. Phys. Express,* vol. 10, no. 6, pp. 065501, 2017.
[23] S. Vura *et al.*, "Epitaxial $BaTiO_3$ on Si (100) with In-Plane and Out-of-Plane Polarization Using a Single TiN Transition Layer," *ACS Appl. Electron. Mater.,* vol. 3, no. 2, pp. 687-695, 2021.
[24] A. Meier, F. Niu, and B. Wessels, "Integration of $BaTiO_3$ on Si (001) using MgO/STO buffer layers by molecular beam epitaxy," *J Cryst. Growth,* vol. 294, no. 2, pp. 401-406, 2006.
[25] T. Zhao *et al.*, "Enhancement of second-harmonic generation in $BaTiO_3/SrTiO_3$ superlattices," *Phys. Rev. B,* vol. 60, no. 3, pp. 1697, 1999.
[26] E. Kim *et al.*, "Second-harmonic generation of single BaTiO3 nanoparticles down to 22 nm diameter," *ACS Nano,* vol. 7, no. 6, pp. 5343-5349, 2013.
[27] B. Bihari, J. Kumar, G. T. Stauf *et al.*, "Investigation of barium titanate thin films on MgO substrates by second-harmonic generation," *J. Appl. Phys.,* vol. 76, no. 2, pp. 1169-1174, 1994.
[28] T. Jin *et al.*, "Mid-infrared chalcogenide waveguides for real-time and nondestructive volatile organic compound detection," *Anal. Chem.,* vol. 91, no. 1, pp. 817-822, 2018.
[29] J. Zhou, and P. T. Lin, "Midinfrared Multispectral Detection for Real-Time and Noninvasive Analysis of the Structure and Composition of Materials," *ACS Sensors,* vol. 3, no. 7, pp. 1322-1328, 2018.
[30] P. T. Lin *et al.*, "Label-free glucose sensing using chip-scale mid-infrared integrated photonics," *Adv. Opt. Mater.,* vol. 4, no. 11, pp. 1755-1759, 2016.
[31] A. Lochbaum *et al.*, "On-chip narrowband thermal emitter for mid-IR optical gas sensing," *ACS Photonics,* vol. 4, no. 6, pp. 1371-1380, 2017.
[32] S. Borri *et al.*, "High-precision molecular spectroscopy in the mid-infrared using quantum cascade lasers," *Appl. Phys. B,* vol. 125, no. 1, pp. 1-9, 2019.
[33] Q. Hao *et al.*, "Mid-infrared transmitter and receiver modules for free-space optical communication," *Appl. Opt.,* vol. 56, no. 8, pp. 2260-2264, 2017.
[34] H. D. Megaw, "Origin of ferroelectricity in barium titanate and other perovskite-type crystals," *Acta Crystallographica,* vol. 5, no. 6, pp. 739-749, 1952.
[35] S. A. Denev *et al.*, "Probing ferroelectrics using optical second harmonic generation," *J. Am. Ceram. Soc.,* vol. 94, no. 9, pp. 2699-2727, 2011.
[36] J. Zhou *et al.*, "Broadband mid-infrared second harmonic generation using epitaxial polydomain barium titanate thin films," *Photonics Res.,* vol. 7, no. 10, pp. 1193-1199, 2019.
[37] O. Diéguez, K. M. Rabe, and D. Vanderbilt, "First-principles study of epitaxial strain in perovskites," *Phys. Rev. B,* vol. 72, no. 14, pp. 144101, 2005.